

# Scan Angle Stability of a Second-Order Plasma-Switched Frequency Selective Surface

Lee W. Cross\*<sup>1</sup> and Mohammad J. Almalkawi<sup>2</sup>

<sup>1</sup>Imaging Systems Technology, Toledo, Ohio, USA

<sup>2</sup>EECS Department, College of Engineering, University of Toledo, Toledo, Ohio, USA

\*Corresponding author: 4750 W. Bancroft St., Toledo, OH 43615, [lcross@teamist.com](mailto:lcross@teamist.com)

**Abstract:** Large-area, light-weight electromagnetic protection (EP) structures are needed to protect sensitive microwave sensors and communications systems from high-power microwave (HPM) and electromagnetic pulse (EMP) threats. This paper presents the use of COMSOL Multiphysics for electromagnetic simulation of a plasma-based frequency selective surface (FSS) structure that can provide significant shielding in harsh environments. The second-order structure contains encapsulated plasma elements, with plasma modeled as homogeneous negative permittivity dielectric material, and is transparent at X-band in the off state and blocks energy in the on state. Performance of an infinite array was simulated using Floquet boundary conditions. Off state performance is stable in terms of frequency and bandwidth across wide incidence (scan) angles, and significant switchable attenuation is predicted in the on state. Simulation time is shown versus number of cores on a 16-core Xeon server. Electromagnetic performance for this structure is excellent, and COMSOL will be used to model additional physics domains in future work.

**Keywords:** bandpass filter, Floquet port, frequency selective surface, plasma, scan stability.

## 1. Introduction

Frequency selective surfaces (FSS) are used in many radio frequency (RF) applications including sensors, radar, and communications systems in order to provide large surfaces with tailored electromagnetic (EM) properties [1]. RF systems are vulnerable to damaging levels of EM radiation from unintentional sources such as high-power tracking radars and interference from nearby transmitters, and intentional sources such as high-power microwave (HPM) and electromagnetic pulse (EMP) weapons and high-

altitude EMP (HEMP) bursts from nuclear explosions [2–3].

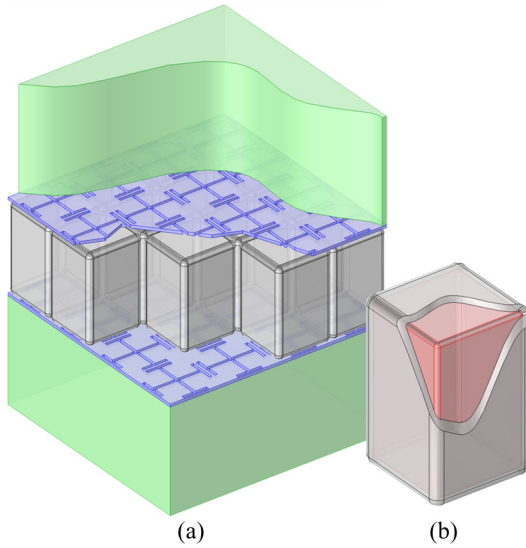
There is significant opportunity to increase system functionality, survivability, and payload by integrating switchable protective structures into existing EM surfaces. Many platforms also require extremely rugged components that can withstand extreme temperatures, ionizing radiation, and corrosive environments. Past attempts at developing switchable plasma apertures resulted in devices that were fragile, size-limited, or required bulky power sources [4–5]. Recent work with ceramic encapsulated plasma devices may overcome these limitations [6].

In this paper, COMSOL Multiphysics 4.3b was used to simulate the EM performance of a second-order bandpass FSS that includes an array of gas-filled plasma-shells. The EM aperture can be effectively closed by controlling plasma electron density within these shells, thereby shielding sensitive sensors from incident EM threats.

This paper is organized as follows. Section 2 presents the plasma-shell FSS structure and describes its theory of operation. Section 3 describes the construction of the COMSOL simulation model. Section 4 presents simulation results of the model meshing study, simulation time on a 16-core dual processor server, and EM performance in the on and off state across scan angle. Section 5 summarizes the work and discusses future directions for the research.

## 2. Proposed Structure

The proposed structure consists of an array of unit cells shown in Figure 1(a). The outer dielectric layers (green) are a low-dielectric-constant material and are laminated to conductive FSS layers (blue) that are patterned with Jerusalem cross slots. The elements are resonant at 10 GHz (e.g., in X-band) and act as spatial bandpass filter elements. The conductive layers can be fabricated by electroplating and



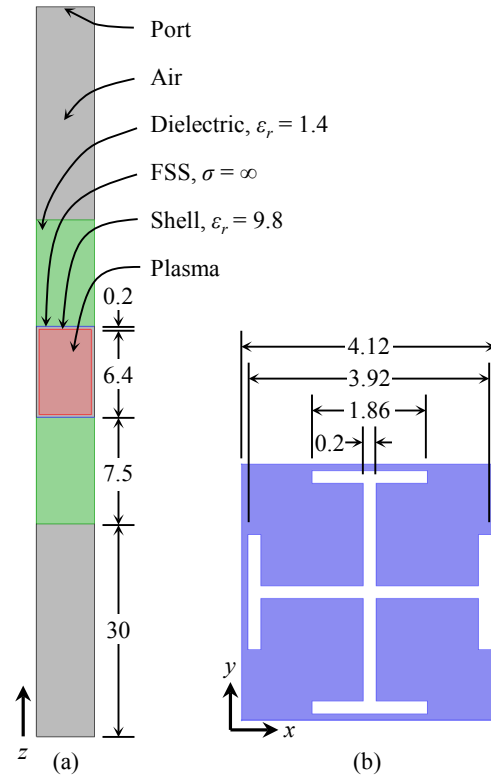
**Figure 1.** (a) Successive layers of the proposed structure are shown in (a), composed of outer dielectric layers (green) encasing two FSS layers (blue) and an array of plasma-shells (gray). (b) A section of the plasma-shell shows internal plasma (red).

photo etching processes, or using patterned conductive silver paint.

FSS layers are bonded onto an array of close-packed plasma-shells. Plasma-shells are tiny gas encapsulating structures that can be used as building blocks to form novel RF structures, shown in Figure 1(b) sectioned to show internal plasma (red). Depending on how it is controlled, the encapsulated plasma will absorb, reflect, or transmit incident energy and is useful in many RF applications. FSS layers can be driven with an external high-voltage ac power source to ionize gas within the shells. Plasma directly interacts with propagating EM energy to accomplish switchable transmission and high-power isolation.

Complete geometry of the unit cell is shown in Figure 2 along with dimensions and material properties. The profile view shows the symmetrical structure and it should be noted that several features contribute to stability at wide scan angles (scan independence): low-permittivity outer and inner dielectric slabs with guided wavelength  $\lambda$  of  $\sim 0.3 \lambda$ , and small closely spaced FSS elements with strong mutual coupling.

The plasma volume within each plasma-shell can be modeled as a homogeneous conductive



**Figure 2.** Unit cell geometry: (a) profile view showing air box, dielectric (green), shell, and plasma (red); and (b) FSS Jerusalem cross element (all units mm).

dielectric medium. Complex permittivity is defined as  $\epsilon = \epsilon_0(\epsilon_r' - j\epsilon_r'')$ , consisting of real and imaginary relative permittivity ( $\epsilon_r'$  and  $\epsilon_r''$  respectively), and both frequency-dependent components for a cold, collisional, and weakly ionized plasma are

$$\epsilon_r' = 1 - \frac{\omega_p^2}{\omega^2 + \nu^2}, \text{ and} \quad (1)$$

$$\epsilon_r'' = \frac{\omega_p^2 \nu / \omega}{\omega^2 + \nu^2}, \quad (2)$$

as functions of plasma frequency ( $\omega_p$ , in rad/s), microwave drive frequency ( $\omega$ , in rad/s), and electron collision frequency ( $\nu$ , in rad/s) [7]. Plasma conductivity  $\sigma$  is a frequency invariant parameter. This study uses plasma parameters derived from previous experimental work with the following values:  $\sigma = 0.45$  S/m,  $\omega_p = 1.07 \times 10^{11}$  rad/s (based on electron density  $n_e$  of  $3.6 \times 10^{12}$  cm $^{-3}$ ), and  $\nu = 4.3 \times 10^9$  rad/s [4].

**Table 1.** Global parameters

Name	Expression	Description
$f_{min}$	7[GHz]	Min. sweep frequency
$f_{max}$	13[GHz]	Max. sweep frequency
$\alpha_{phal}$	0[deg]	Elevation incidence angle
$pol$	1	Polarization: 1=par., 0=orth.
$n_e$	0	Plasma density, $cm^{-3}$

### 3. Use of COMSOL Multiphysics

EM Floquet port simulations can be done in COMSOL with either the RF or Wave Optics Module, and this study used the former physics module with a frequency domain analysis.

After capturing the model geometry, the parameters in Table 1 were added to enable parametric sweeps. The frequency dependent components of plasma permittivity in (1) and (2) were solved in analytic functions that take the arguments of plasma density and COMSOL solution frequency variable  $freq$ .

A series of boundary conditions shown in Figure 3 were applied to the model. First, periodic ports 1 and 2 were assigned to the top and bottom faces, respectively. Each port specified one corner point mirrored about the center of the model. Port 1 wave excitation polarity was defined using the E-field vector expression

$$\mathbf{E}_0 = \begin{pmatrix} \text{if}(pol, \cos(\alpha_1) * \cos(\alpha_2), \sin(\alpha_2)) \\ \text{if}(pol, \cos(\alpha_1) * \sin(\alpha_2), \cos(\alpha_2)) \\ \text{if}(pol, \sin(\alpha_1), 0) \end{pmatrix} \quad (3)$$

that orients incident E-field in the  $x$  direction for either polarization. Wave polarization is defined as E-field oriented either parallel or orthogonal to the plane of incidence, where the incident plane is orthogonal to the port plane and rotated away from the  $x$  axis by azimuth angle  $\alpha_2$ . Elevation angle  $\alpha_1$  measures the angle of the wave vector  $\mathbf{k}$  from the  $z$  axis. The receiving port must be configured similarly but the following variables must be negative because the port normal vector points in the opposite direction:  $\mathbf{E}_0$   $z$  component,  $\alpha_1$ , and  $\alpha_2$ . In addition,  $\alpha_2$  must have a factor of  $\pi/2$  added. The *Compute Diffraction Orders* button should be clicked for both ports prior to simulation whenever  $\alpha_1$  is changed, using the maximum value of  $\alpha_1$  for

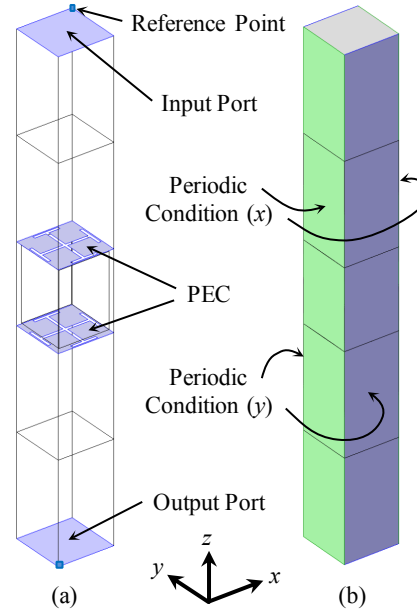


**Figure 3.** Model boundary conditions for (a) periodic ports with reference points, conductive FSS layers; and (b) periodic boundary conditions for Floquet port simulation. Note: the air box is not to scale.

scan angle sweeps. The distance between the wave port and substrate surface was parameterized because it should generally be greater than  $\lambda/4$  at the lowest frequency  $f_{min}$ .

Next, two sets of periodic boundary conditions were assigned to opposing outer surfaces. Last, the FSS layers were assigned the perfect electrical conductor (PEC) boundary condition to model thin conductive sheets.

Prior to assigning material properties for each model domain, the wave equation for electrical displacement field was set to dielectric loss to accommodate the frequency dependent, lossy plasma. Then materials were created for the substrate, shell, and plasma that were subsequently assigned to domains.

Maximum mesh element length of  $\lambda/5$  was used as a starting point, where guided wavelength in dielectric materials is inversely proportional to  $\sqrt{\epsilon_r}$ . Therefore four mesh size nodes were added for the different materials. The relative dielectric constant of plasma was assumed to be  $-2$  for meshing purposes, corresponding to the calculated value at 10 GHz. The periodic boundary conditions require that paired faces have identical meshes, so a free

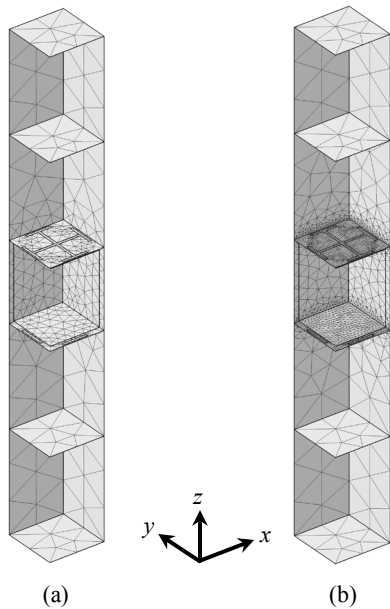


**Figure 4.** (a) Initial and mesh settings were refined at the FSS surface to create (b) an accurate final mesh. Note: the air box is not to scale.

triangular mesh was copied to the opposing side for each periodic boundary pair.

## 4. Results and Discussion

### 4.1 Meshing Study

Initial mesh size in Figure 4(a) was incrementally reduced in order to find convergence in passband performance. To do this, a mesh divisor parameter was added to all mesh size node parameters of maximum and minimum element size. The divisor was incremented from 1 (i.e., the initial mesh size of  $\lambda/5$ ) to 6 in steps of 1. For a frequency sweep of 7–13 GHz with 0.2 GHz steps at normal incidence, the finest mesh required 642 128 degrees of freedom (DOF), 9.3 GB memory, and solved in 1498 s using 8 CPU cores. Bandwidth converged to 15% higher than the initial value and appeared to be a stable solution. As a simple way to reduce the problem size, all meshes were reset to their original sizes and the mesh divisor of 6 was applied to single domains: dielectric, FSS, shell, and plasma. Fine meshing of the FSS layer shown in Figure 4(b) best matched the global refinement, matching center frequency  $f_c$

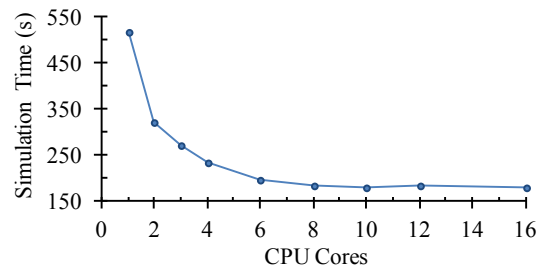


**Figure 5.** Simulation time is minimized using 8 cores.

and bandwidth to within 1%, requiring 130 068 DOF, 2.2 GB memory, and 178 s.

### 4.2 Multi-core Simulation

Simulation time versus number of CPU cores was investigated using a server computer running Windows 7 Pro with two 8-core Intel Xeon E5-2687W processors, 64 GB DDR3-1600 memory, and a solid state hard drive. Simulation time of the previous model is shown in Figure 5 and no further speedup is evident using more than 8 cores. The computer can be efficiently utilized with this model by partitioning sweeps into multiple COMSOL windows and solving simultaneously.

### 4.3 Scan Stability

Wide scan angle transmission performance was simulated around the passband by performing a parametric sweep of  $\alpha_1$  up to  $70^\circ$ , both polarizations, with and without plasma. Figure 6 shows that the stable 3 dB bandwidth across scan angle and polarization is only 29% less than the nominal response at normal incidence. This level of performance is critical for high-performance systems that operate over wide scan angles. Average switchable attenuation in the passband is 18.4 dB, and this provides a significant level of protection and RF isolation.

### 4.4 Wideband Response

Wideband performance was examined by performing a parametric sweep of two incidence angles:  $0^\circ$  and  $45^\circ$ , with both polarizations in the off and on state. Figure 7 confirms good out-of-band rejection below the passband and up to the first spurious passband at 18.5 GHz. The null at

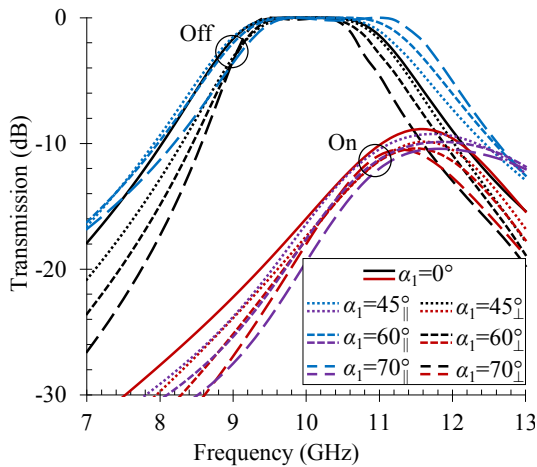


**Figure 6.** Transmission performance of the structure shows scan stability up to  $70^\circ$  for all polarizations and 3 dB bandwidth of 1.73 GHz at 9.93 GHz. Average on-state attenuation is 18.4 dB.

14 GHz for orthogonal polarization is a characteristic of the Jerusalem cross element. It may be possible to push the null 1–2 GHz higher, but a different FSS element design would be needed to eliminate it entirely. The first spurious passband is widely separated at 18.5 GHz. On-state attenuation shows evidence of the null at 14.5 GHz but is otherwise well behaved and shows significant additional rejection across all frequencies.

#### 4.5 Field Visualization

Jerusalem cross elements concentrate propagating RF energy within the slots where it interacts with confined plasma. Figure 8 shows the normalized E-field through the center of the model (in the  $xz$  plane). In Figure 8(a), energy passes through the structure in the off state and E-fields are constant outside the structure. E-field is very high but constant at both FSS elements. In Figure 8(b), the top FSS surface reflects incident energy in the on state and this is seen as a large standing wave near the input port. What little energy that propagates through the plasma is further attenuated by the bottom FSS element. The E-field concentration within the Jerusalem cross element is shown in Figure 8(c), and this effect enhances plasma shielding.

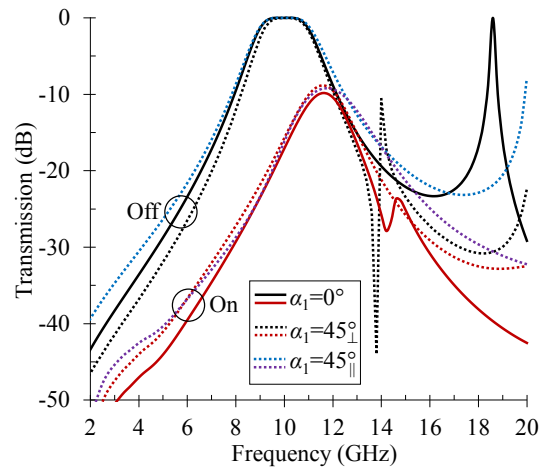


**Figure 7.** Wideband frequency response shows a null outside the passband at 14 GHz and first spurious response at 18.5 GHz.

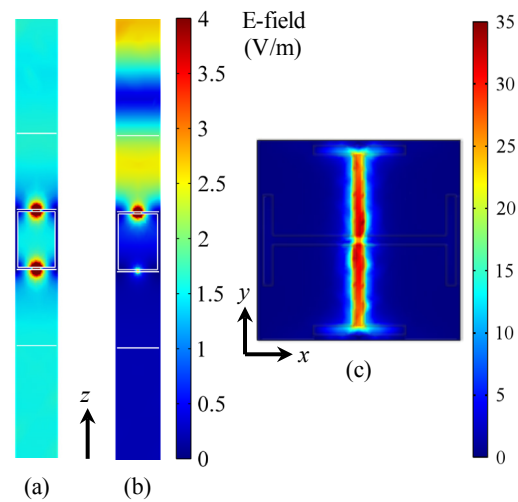


**Figure 8.** Normalized E-field at 10 GHz ( $xz$  plane) in the off state (a) shows energy passing through the structure. In the on state (b), plasma reflects incident energy and large standing waves at the input (top) side are seen. Significant voltage multiplication is shown at the top FSS in (c) in the off state.

#### 5. Conclusions

Plasma-shells are an engineered material capable of directly integrating into existing structures to allow implementation of low-loss HPM/EMP protection. IST has used plasma-shell RF properties in previous research to implement planar microwave filter-limiters, large-area plasma apertures, and FSS limiters. Multiphysics

modeling of these devices will enable a simulation-based design approach for these novel structures. Possible future applications of plasma-shells in RF structures include plasma-based metamaterials, reflectarrays with integral HPM/EMP protection, waveguide filter-limiters, high- $Q$  filter-limiters, and other plasma-tunable devices.

## 6. References

1. B. A. Munk, *Frequency selective surfaces*, Wiley Interscience, New York (2000)
2. M. G. Bäckström and K. G. Lövstrand, "Susceptibility of electronic systems to high-power microwaves: Summary of test experience," *IEEE Trans. Electromagn. Compat.*, **vol. 46**, no. 3, pp. 396–403 (2004)
3. J. Benford et al., *High power microwaves*, Taylor & Francis (2007)
4. R. J. Vidmar, "On the use of atmospheric pressure plasmas as electromagnetic reflectors and absorbers," *IEEE Trans. Plasma Sci.*, **vol. 18**, no. 4, pp. 733-741 (1990)
5. T. Anderson et al., "Plasma frequency selective surfaces," *IEEE Plasma Sci.*, **vol. 35**, no. 2 (2007)
6. L. W. Cross et al., "Development of large-area switchable plasma device for X-band applications," *IEEE Trans. Plasma Sci.*, **vol. 41**, no. 4, pp. 948-954 (2013)
7. J. P. Rybak, "Causes, effects and diagnostic measurements of the reentry plasma sheath," Rep., Colorado State Univ., Fort Collins, CO (1970)